Eidgenössische Technische Hochschule Zürich
Swiss Federal Institute of Technology Zurich

Characterization of a phaseplate for the creation of a tophat potential

Semester Project

Nicolò Montalti
nmontalti@student.ethz.ch

Quantum Optics Group
Departement of Physics, D-PHYS
ETH Zürich

Supervisor:
Prof. Tilman Esslinger

Advisors:
Dr. Meng-Zi Huang
Mohsen Talebi

July 9, 2023

Abstract

Contents

Chapter 1

Introduction

Predicting the behaviour of complex systems has always been an important goal of scientific research. From predicting the motion of stars and planets in our solar system, to understanding the behaviour of complex systems showing chaotic behaviours. In history, before scientists were able to find analytical solutions to many problems, they often relied on simulations. A celebrated example are the astronomical clocks that were built in Asia and Europe in the period between 1000 and 1500, such as the famous astronomical clock in Prague (1410) or the Zytglogge in Bern (1530). They were used to predict the position of the planets and the constellations, the phases of the moon and its eclipses [1].

With the advent of quantum mechanics, a new kind of problems for which no analytical solution is possible was found. Given the high dimensionality of the Hilbert space, classical computers cannot be used to find numerical solutions to quantum many body problems. For example, simulating a system of $N = 36$ qubit using two double-precision floating-point numbers to store a complex number, would require approximately $2^{N+1} \times 8$ byte $= 1$ Terabyte of memory. For every additional qubit, this number would double.

Richard Feynman was the first to propose to use a quantum system to handle this complexity making use of the law of quantum mechanics itself. In 1982, he proposed to make use of "one controllable quantum system [to] simulate another" [2]. In this way, a system of N quantum particles could be simulated using another system of N qubits. The problem is then moved to finding a system that can be easily tuned and controlled, such that it can be used to simulate a wide range of problems.

1.1 Analog and digital quantum simulation

Two different approaches have arisen in the past years: (digital) quantum computation and (analog) quantum simulation. In the first case, the information is encoded in qubits that can be in two computational states $|0\rangle$ and $|1\rangle$. In the latter, a direct mapping between the original problem (i.e. its Hamiltonian) and the simulating system is realized. Among the most promising platforms for quantum computation, we cite the use of superconducting circuits [3], Rydberg atoms [4] and trapped ions [5]. Whereas for quantum simulation, the use of ultracold quantum gases has become increasingly popular [1].

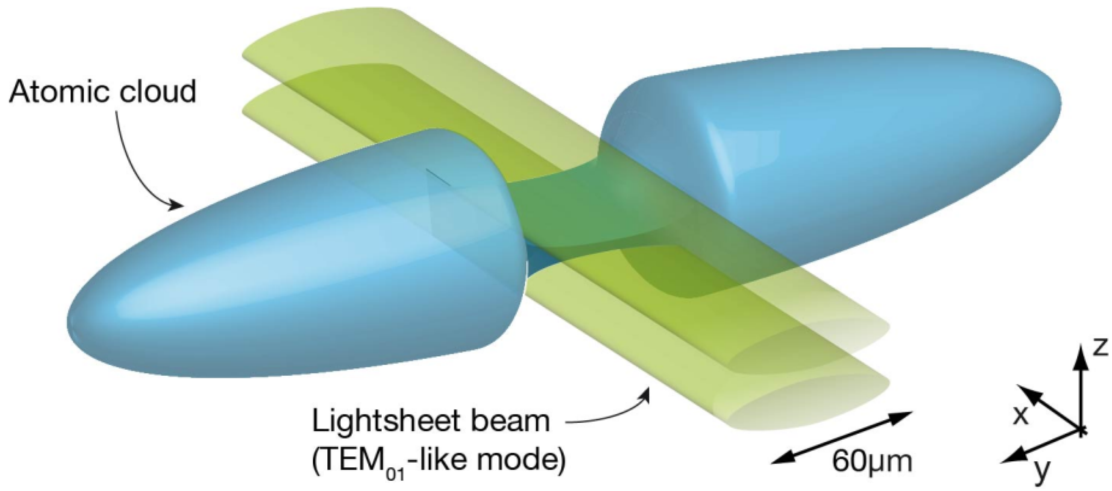

Figure 1.1: *Experimental setup. A cloud of atoms is trapped in a cigar-shaped potential. A blue-detuned TEM_{01} laser mode propagating in the x direction defined a quasi-2D channel connecting two smoothly connected reservoirs. Figure from Krinner [13].*

For example, a system of electrons moving in an ionic periodic lattice potential, can be simulated using a gas of fermionic atoms trapped in an optical lattice potential. Here, the periodic potential through which the particles move is generated externally by making use of the interference pattern of overlapping laser beams [6]. It is performing an experiment of this kind that Bloch oscillations, predicted in 1929 by Felix Bloch [7], were directly observed in 1996 in a cloud of ultracold Caesium atoms [8], after being observed in 1992 through the emission of THz radiation by the electrons in a semiconductor super lattice [9].

In the following years, new interesting experiments were proposed to simulate the behaviour of different quantum systems. Among them, we cite the use of optical lattices to investigate insulating and superfluid quantum phases [10], the use of cavities to mediate long range interactions [11] and the observation of quantized conductance in neutral matter [12]. We will focus on this last experiment, since my project was related to it.

1.2 Transport experiments

Transport experiments study the transport properties of particles moving from one reservoir to another. Krinner *et al.* reported the observation of quantized conductance in the transport of neutral atoms driven by a chemical potential bias [12]. Their experiment let them investigate quantum conductors with wide control not only over the channel geometry, but also over the reservoir properties, such as interaction strength, size and thermalization rate.

The basic setup of the experiment is shown in Fig. 1.1. A cloud of atoms is radially trapped with a dipole trap realized with a red-detuned laser. Along the y axis the confinement is produced by the magnetic field curvature of the Feshbach coils. This defines a cigar-shaped cloud elongated in the y direction. The cloud is then split in two reservoir connected by a

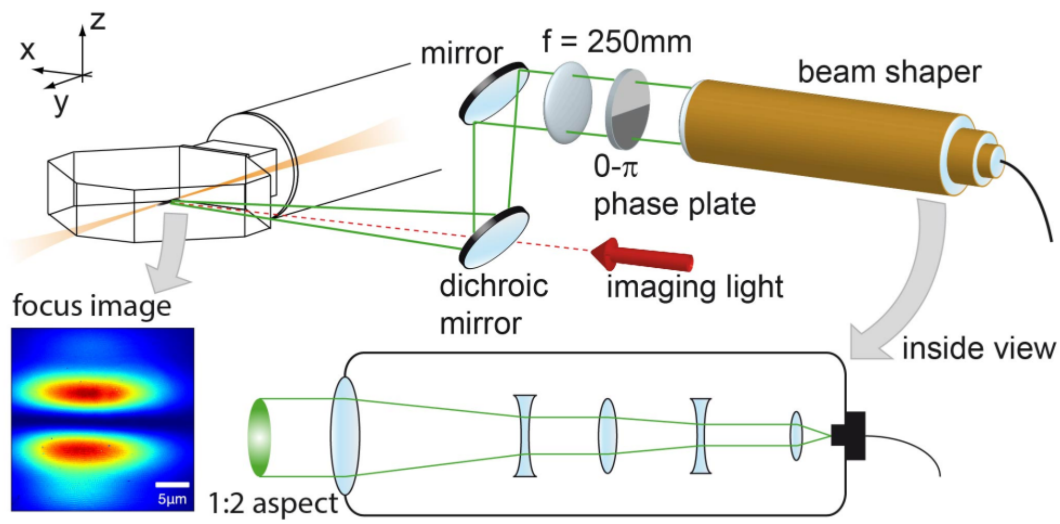

Figure 1.2: *Generation of the* TEM_{01} *mode for the creation of 2D channel. A set of spherical and cylindrical lenses is used to expand the beam in the* z *direction. The beam is then sent to a* $0-\pi$ *phase plate and focused through a* 250 mm *lens on the atomic cloud. Figure from Krinner [13].*

quasi-2D channel sending a blue-detuned TEM_{01} laser mode in the x direction. The blue-detuned laser creates a repulsive potential that confines the atoms in a quasi-2D region. The experiment is then carried on creating a chemical potential imbalance between the two reservoir and studying the conduction of atoms between them. Different experiments can be realized creating a temperature imbalance or a spin imbalance between the reservoirs.

The focus of this thesis is on the blue-detuned laser generating the 2D channel. In the current experiment, the laser is in a TEM_{01} mode. The beam is shaped through a series of optical components shown in Fig. 1.2. It is clear that the potential inside the channel region is not uniform along the y direction. The conductance is influenced by this varying potential and it would be desirable to have a uniform region connecting the two reservoir.

The opportunity to create such a uniform 2D channel was previously investigated by Moritz Schmidt in his semester project [14]. Schmidt considered two options for generating a uniform light sheet: the use of liquid-crystal spatial light modulators and of custom-made glass $0-\pi$, top-hat phase-plates. It was found that this second option is more suitable to the experiment, being at the same time able to satisfy the experimental requirements and considerably cheaper.

1.3 Outline

In this report, I analyse and characterize the custom-made phase plate ordered for the creation of the uniform light sheet. I will start by reviewing the theory behind spatial light modulation, focusing on how a phase plate can be used to shape light beams. Then I will present the apparatus used to characterize the phase plate and the results.

Chapter 2

Theoretical background

In this chapter we focus on how we can generate an arbitrary potential for our cloud of ultracold atoms. To understand it, we first need to review the basics of quantum optics that explain how atoms and light interact, resulting in a dipole force that can be used to trap the atoms. We then focus on the theory of spatial light modulation. For it, we will present a discussion on Fourier optics and use it to understand how a phase plate can be used for such a purpose.

2.1 Atom-light interaction

It is well known that atoms can interact with light. At the quantum level, the interaction is usually interpreted as the absorption or emission of photons by the atoms. Despite this picture being accurate, matter can also interact with light through virtual absorption or emission processes, that result in interesting behaviours. For this to happen, the frequency of light must be far detuned from the excitation energy of the atoms. An important effect of this type of interaction is the dipole force exerted by light on atoms. To understand the origin of this force, it is sufficient to remember that photons, besides energy, also carry momentum. When a photon is scattered by an atom, its momentum is transferred, generating an effective force that acts on the latter.

2.1.1 The dipole force

To study this force in more detailed, we model the atom as a two level system, where the energy levels are separated by an energy $\hbar\omega_{eg}$. We also consider light made of a single mode of frequency $\omega/2\pi$, like the light emitted by a laser. The following discussion is adapted from Jonathan Home's lecture notes on Quantum Optics.

We start by writing the interaction Hamiltonian in the dipole approximation

$$H_{\text{int}} = \boldsymbol{d} \cdot \boldsymbol{E}(\boldsymbol{r}) \tag{2.1}$$

where $\boldsymbol{d}$ is the dipole moment operator, $\boldsymbol{E}$ the electric field and $\boldsymbol{r}$ the position of the atom. The Hamiltonian of the atom without the interaction term is

$$H_0 = \frac{\hbar\omega_{eg}}{2}\sigma_z + \frac{\boldsymbol{p}^2}{2m} \tag{2.2}$$

where σ_z is the third Pauli matrix and $\boldsymbol{p}$ is the momentum operator. Furthermore, we consider a classical electric field

$$\boldsymbol{E} = \frac{1}{2} E_0 f(\boldsymbol{r}) \left(e^{i(\boldsymbol{k}\cdot\boldsymbol{r}-\omega t)} + e^{-i(\boldsymbol{k}\cdot\boldsymbol{r}-\omega t)} \right) \boldsymbol{\epsilon} \tag{2.3}$$

where E_0, ω and $\boldsymbol{\epsilon}$ are the field strength, frequency and polarization respectively. The function $f(\boldsymbol{r})$ allows the field amplitude to vary spatially. The interaction Hamiltonian can be rewritten as

$$H_{\text{int}} = (\boldsymbol{\mu}_{eg} \cdot \hat{\boldsymbol{\epsilon}} E_0) \frac{f(\boldsymbol{r})}{2} (\sigma_+ + \sigma_-) \left(e^{i(\boldsymbol{k}\cdot\boldsymbol{r}-\omega t)} + e^{-i(\boldsymbol{k}\cdot\boldsymbol{r}-\omega t)} \right) \tag{2.4}$$

where $\mu_{eg} = \langle e| \boldsymbol{d} |g\rangle$. It is useful to move to the rotating frame with respect to the laser frequency. After transforming the Hamiltonian and performing the rotating wave approximation, we are left with

$$H = -\frac{\hbar\delta}{2}\omega_z + \frac{\boldsymbol{p}^2}{2m} + \frac{\hbar\Omega(\boldsymbol{r})}{2} \left(\sigma_+ e^{i\boldsymbol{k}\cdot\boldsymbol{r}} + \sigma_- e^{-i\boldsymbol{k}\cdot\boldsymbol{r}} \right) \tag{2.5}$$

with $\Omega(\boldsymbol{r}) = \boldsymbol{\mu}_{eg} \cdot \hat{\boldsymbol{\epsilon}} E_0 f(\boldsymbol{r})/\hbar$ and $\delta = \omega - \omega_{eg}$.

We can find the resulting force applied on the atom by using Heisenberg's equation of motion

$$\begin{aligned} \boldsymbol{F} = \frac{\mathrm{d}\boldsymbol{p}}{\mathrm{d}t} = \frac{i}{\hbar} [H, \boldsymbol{p}] \\ = -\frac{\hbar}{2} \nabla\Omega(\boldsymbol{r}) \left(\sigma_+ e^{i\boldsymbol{k}\cdot\boldsymbol{r}} + \sigma_- e^{-i\boldsymbol{k}\cdot\boldsymbol{r}} \right) - \frac{\hbar}{2} \Omega(\boldsymbol{r}) i\boldsymbol{k} \left(\sigma_+ e^{i\boldsymbol{k}\cdot\boldsymbol{r}} - \sigma_- e^{-i\boldsymbol{k}\cdot\boldsymbol{r}} \right) \end{aligned} \tag{2.6}$$

We observe that we get two terms. The first, proportional to the spatial derivative of the field strength, includes a contribution in phase with the light field. It is the term that results in the dipole force exerted by the field on the atom, the one we are interested in. The second term is proportional to the field strength, and it is out of phase of a factor of π with respect to the field. It is responsible for the scattering force, essential for cooling atoms. The second term is dominated by the first for large detuning δ, and it will then be neglected in the following discussion.

We will now make use of two approximation to simplify the calculations. We first make use of a mean-value approximation for the centre-of-mass degree of freedom. This means that we evaluate the internal states operators appearing in $\mathrm{d}\boldsymbol{p}/\mathrm{d}t$ using the mean position $\boldsymbol{r} = \langle \boldsymbol{r} \rangle + \langle \boldsymbol{v} \rangle t$, where $\boldsymbol{v}$ is the velocity of the atom. Moreover, since the timescale on which the internal degrees of freedom of the atom evolve are much faster than the timescale associated to the movement of it, we only consider the steady state solution of the atomic dynamics.

Making use of the approximations explained above, in the limit $\delta \gg \Omega, \Gamma$, where Γ is the decay rate, we find

$$\boldsymbol{F}_{\text{dip}} = \left\langle \frac{\mathrm{d}\boldsymbol{p}}{\mathrm{d}t} \right\rangle = -\frac{\hbar}{2} \frac{\Omega}{\delta} \nabla\Omega \tag{2.7}$$

We notice that the dipole force is proportional to the field strength and its gradient, and inversely proportional to the detuning. Moreover, its sign depends on the sign of the detuning. Red-detuned light ($\delta < 0$) generates an attractive potential and can be used to create optical tweezers. This is exploited in our experiment for the creation of the cigar-shaped cloud. On the other hand, blue-detuned light ($\delta > 0$) generates a repulsive potential. This is what we need for the creation of the 2D channel. In the experiment, we use a 660 nm laser, blue-detuned with respect to the Lithium atomic transition of 671 nm.

2.2 Spatial light modulation

Now that we know how light interacts with atoms, we are interested in the techniques that can be used to arbitrary shape a light beam. At the basis of these techniques there is Forier optics, which will be explained in the next section. We will then look at the different tools that can be used to achieve this goal, focusing on the use of phaseplates.

2.2.1 Fourier optics

Fourier optics is essential to understanding how spatial light modulation works. The basic idea is that a lens returns the Fourier transform of an incident beam on its focal plane. This can be used to transform a phase modulation in an intensity modulation. We will now look at this concept in more detail, providing a short introduction to Fourier optics adapted from Saleh and Teich [15] and Schmidt's previous work [14].

Let's suppose we have a monochromatic wave of wavelength λ propagating in the z direction. In the $z = 0$ plane, we can denote its complex amplitude with a function $f(x, y)$. The function $f(x, y)$ can be Fourier transformed and decomposed in plane waves propagating in the x and y directions

$$f(x, y) = \int \mathrm{d}\nu_x \mathrm{d}\nu_y F(\nu_x, \nu_y) e^{-2\pi i(\nu_x x + \nu_y y)} \tag{2.8}$$

where $\nu_x = k_x/2\pi$, $\nu_y = k_y/2\pi$ and

$$F(\nu_x, \nu_y) = \int \mathrm{d}x\mathrm{d}y f(x, y) e^{2\pi i(\nu_x x + \nu_y y)} \tag{2.9}$$

Each plane wave travels in a direction $\theta_x = \sin^{-1}(k_x/k) = \sin^{-1}(\lambda\nu_x)$ and $\theta_y = \sin^{-1}(k_y/k) = \sin^{-1}(\lambda\nu_y)$ and has an amplitude $F(\nu_x, \nu_y)$

One way to separate the Fourier components of a wave is by using a lens. A thin spherical lens transforms a plane wave incident on it into a paraboloidal wave focused on a point on the focal plane of the lens (Saleh and Teich Sec. 2.4 [15]). As shown in Fig. 2.1, a plane wave incident at a small angle (θ_x, θ_y) if focused to the point $(x, y) = (\theta_x f, \theta_y f)$, where f is the focal length of the lens. The complex amplitude $g(x, y)$ at $z = f$ is therefore proportional to the Fourier transform of $f(x, y)$ evaluated at $\nu_x = x/\lambda f$ and $\nu_y = y/\lambda f$.

$$g(x, y) \propto F\left(\frac{x}{\lambda f}, \frac{y}{\lambda f}\right) \tag{2.10}$$

To find the proportionality factor, we trace the propagation of every plane wave in which we have decomposed the input beam through the optical system. Then we integrate over all

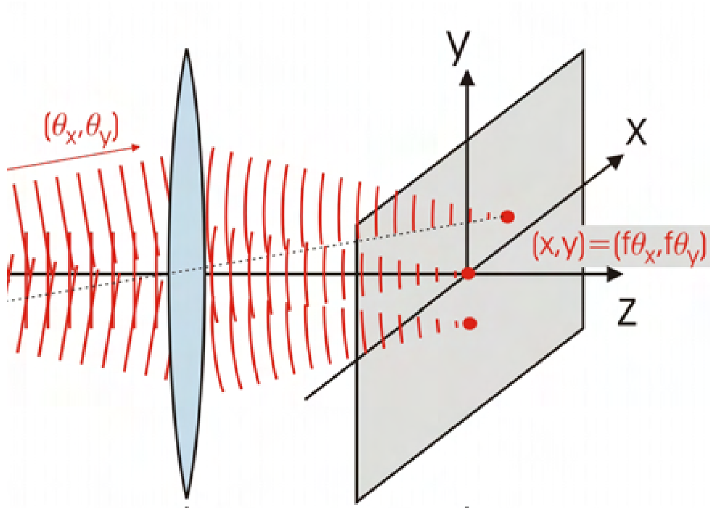

Figure 2.1: *Focusing of a plane wave into a point. A direction (θ_x, θ_y) is mapped into a point $(x, y) = (\theta_x f, \theta_y f)$. The lens in positioned at $z = 0$ and the focal plane at $z = f$. Image from Heine [16]*

.

these plane waves at the output to obtain $g(x, y)$. In the following, we will make use of the Fresnel and paraxial approximations.

A field $F(k_x, k_y)$ can be propagated from the $z = 0$ plane to the $z = f$ plane by applying a phase factor $e^{-ik_z z}$

$$G(k_x, k_y) = F(k_x, k_y)e^{-ik_z z} = H(k_x, k_y, z)F(k_x, k_y) \tag{2.11}$$

with $k_z = \sqrt{k^2 - k_x^2 - k_y^2}$ and $H(k_x, k_y, z) = e^{-ik_z z}$. We can now perform the Fresnel approximation, which states that for plane waves travelling at small angles $(k_x, k_y \ll k)$,

$$H(k_x, k_y, z) = e^{-ik_z z} = e^{-iz\sqrt{k^2-k_x^2-k_y^2}} \approx e^{-ikz}e^{i\frac{k_x^2+k_y^2}{2k}z} \tag{2.12}$$

H is defined in the Fourier space, so we can bring it back to the real space applying an inverse Fourier transform

$$h(x, y, z) = \mathcal{F}^{-1}(H(k_x, k_y, z)) = \frac{i}{\lambda z}e^{-ikz}e^{ik\frac{x^2+y^2}{2z}} \tag{2.13}$$

Now we have to take into account the effect of the lens on the beam. A parabolic lens of focal length f will apply a phasor $\phi(x, y) = \exp\left(-ik\frac{x^2+y^2}{2f}\right)$ in addition to the phase acquired by the propagation of the beam. Overall, at $z = f$

$$g(x, y) = h(h, y, f) \otimes [\phi(x, y)f(x, y)] = \frac{i}{\lambda f}e^{-ikf}F\left(\frac{x}{\lambda f}, \frac{y}{\lambda f}\right) \tag{2.14}$$

The proportionality factor is therefore found to be $1/\lambda f$ and the intensity $I(x, y)$ at the focal plane

$$I(x, y) = \frac{1}{(\lambda f)^2}\left|F\left(\frac{x}{\lambda f}, \frac{y}{\lambda f}\right)\right|^2 \tag{2.15}$$

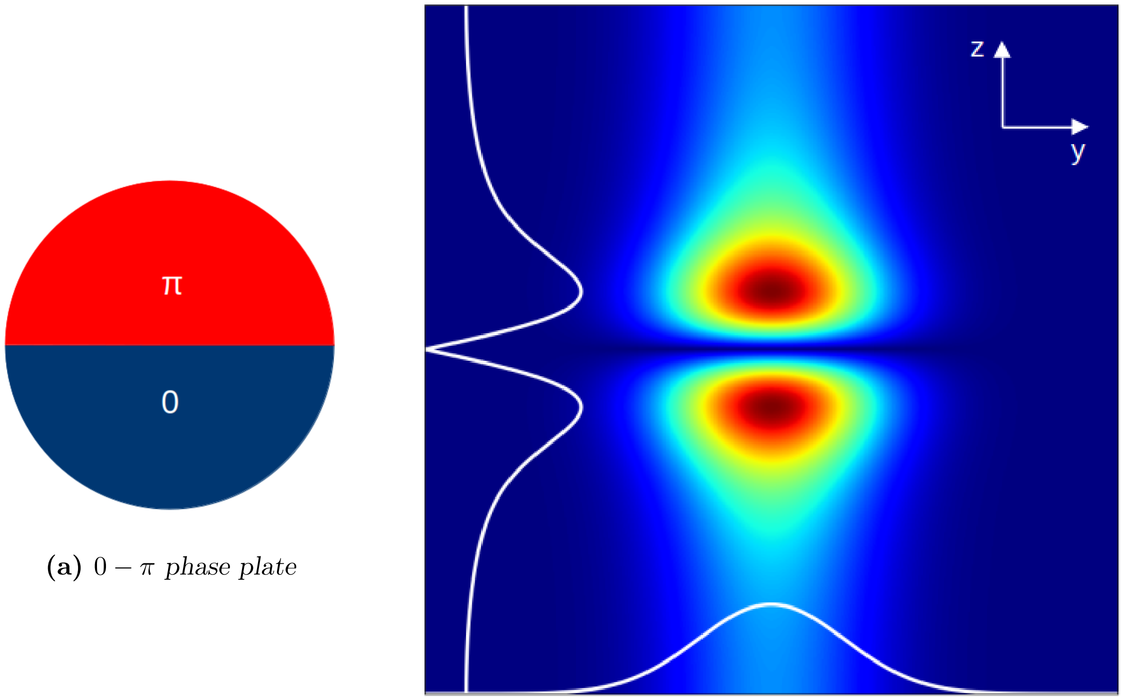

(a) *$0 - \pi$ phase plate*

(b) *TEM_{01} mode*

Figure 2.2: *TEM_{01} mode generated by o $0 - \pi$ phase plate. In the figure on the right, the intensity profile at the focal plane is shown together with the integrated intensity along the two axes.*

To sum up, a lens returns a Fourier transform of the incident beam at a distance equal to the focal length. This can be used to modulate the intensity profile of the beam.

2.2.2 Spatial light modulators: the phase plate

The theory described above can be used as the working principle of numerous devices used for spatial light modulation. Among the ways light can be shaped, it is worth mentioning the use of acusto-optic modulators (AOMs), digital micromirror devices (DMDs), liquid crystals spatial light modulators (LC-SLMs) and phase plates. All these options are good for different purposes. The first three have the advantage of being controllable, allowing the creation of arbitrary shapes simply changing the input signal. The latter is cheaper, but once it has been manufactured, it cannot be modified. The use of an LC-SLM for the creation of a uniform light sheet was investigated by Schmidt in his semester project [14]. However, it was found that a phase plate would offer a cheaper and more reliable alternative. These advantages come at the cost of not having the possibility of changing the phase profile at a later moment.

The working principle of a phase plate is very simple. A wave travelling in a transmissive medium has a lower speed than a wave travelling in air. Designing a plate with variable thickness, it is possible to add an arbitrary phase to a beam. The points where the plate is thicker will be delayed with respect to the points where it is thinner. Placing a lens after the plate will result in the desired intensity modulation at the focal plane.

One of the simplest example of phase plates is the $0-\pi$ phase plate, shown in Fig. 2.2. The plate is divided in two halves, with the upper half out of phase by a factor of π with respect to the lower half. For a beam propagating in the x direction, the phase profile is then (see Fig. 2.2)

$$\phi(y,z) = \begin{cases} 0 & z<0 \\ \pi & z>0 \end{cases} \tag{2.16}$$

This is the phase plate currently used in the experiment, and it generates the TEM_{01} mode shown in Fig. 2.2b.

As it is clear from Fig. 2.2b, the intensity (and therefore the potential) is not uniform along the y direction. On the contrary, it has Gaussian shape, with a peak at the centre. What we would like to achieve is a so-called top-hat potential, shown in Fig. 2.3. It differs from the standard $0-\pi$ phase plate in the y direction. Instead of having a Gaussian profile, it initially ramps up from 0 to 1 (in a.u.), then it remains flat in the central region, and it finally decreases back to 0. In the ramp up region, the profile is Gaussian. In the z direction, it generates the same kind of intensity modulation as the $0-\pi$ phase plate. The region we are interested in is the central region. The phase plate was designed to create an intensity profile as uniform as possible, and this is what we have tried to achieve experimentally.

2.2.3 Required specifications

We now turn our attention towards the specifications that the phase plate has to satisfy in order to be useful for our experiment. The three main aspects we want to focus on are the width of the flat region, the darkness D and the trapping frequency ω_z.

The phase plate was designed to create a flat region of 40 µm, with a ramp up region of 15 µm. The specifications are relative to the intensity profile generated by the phase plate in combination with a lens of focal length $f = 100$ mm. However, in the final experiment it is preferable to use a $f = 250$ mm lens. Therefore all the features will be scaled up by a factor of 2.5. For example the flat region will be 100 µm long instead of 40 µm.

The darkness is the most important parameter of the phase plate. It gives us a measure of how dark is the dark region at the centre of the light sheet compared to the bright region around. Taking inspiration from Krinner's PhD thesis [13], we define it as

$$D = \frac{I_{\mathrm{node}}}{(I_{\mathrm{max},1} + I_{\mathrm{max},2})/2} \tag{2.17}$$

where I_{node} is the intensity at the nodal plane, and $I_{\mathrm{max},1/2}$ is the intensity at the two maxima. For the experiment to work, the darkness has to be on the per mill level. The repulsive laser that creates the 2D channel increases the chemical potential with respects to the reservoirs. If the nodal region is too bright, and therefore the chemical potential too high, the atoms will not be able to pass through the channel, and the transport will be suppressed. According to Krinner's work, for a $0-\pi$ phase plate and typical powers of 1.3 W, a darkness of one per mill increases the chemical potential by 70 nK, and the transport is not suppressed.

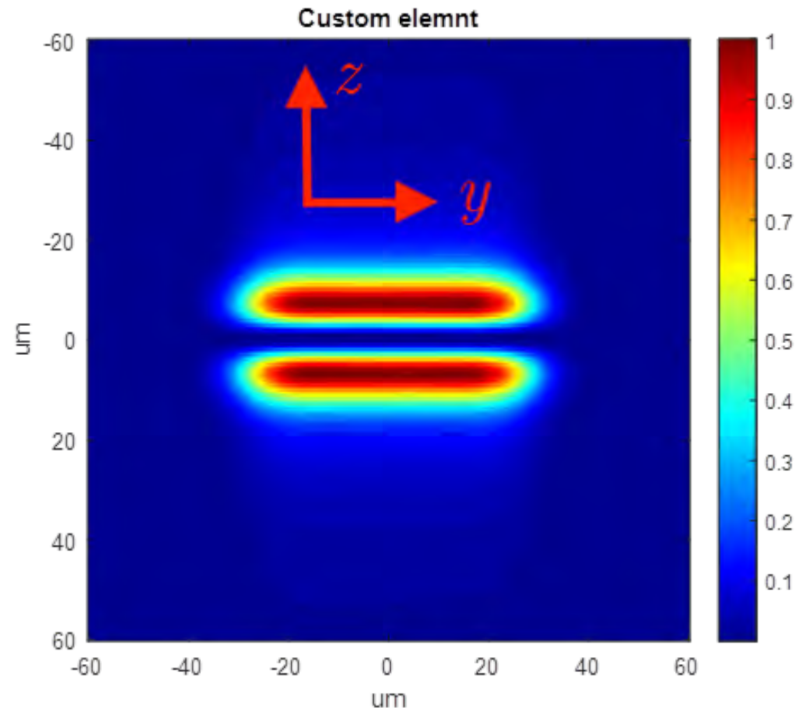

(a) *Beam profile*

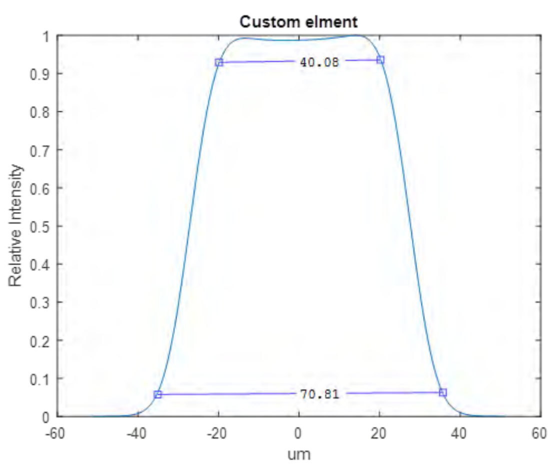

(b) *y direction*

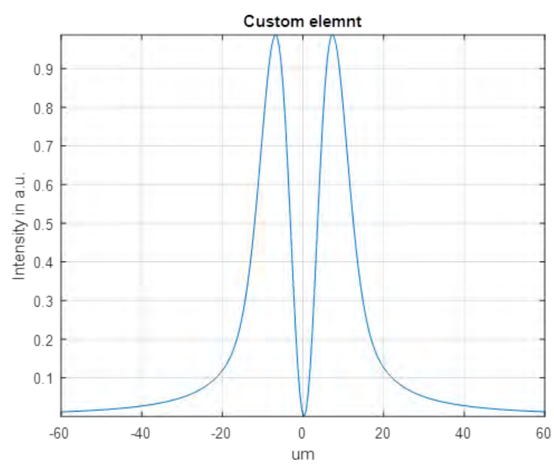

(c) *z direction*

Figure 2.3: *Customized phase plate. In the y direction, the intensity follows a "top hat" profile, characterized by a Gaussian ramping up, a flat region, and a symmetric ramping down. In the z direction, the intensity follows the same profile of a $0 - \pi$ phase plate. The image was provided by Holoor, the manufacturing company.*

In order to freeze-out the z dimension, the trapping frequency must be high enough. If we approximate the trapping potential in the neighbour of the nodal plane with a second order polynomial

$$U(z) = \frac{1}{2} m\omega_z^2 z^2 + \mathcal{O}(z^4) \tag{2.18}$$

we require the trapping energy $\hbar\omega_z$ to be higher than the following energy scales:

- Fermi energy $E_F \approx 600\,\mathrm{nK} = 12.5\,\mathrm{kHz}$
- Binding energy, estimated to be smaller than the 20% of the Fermi energy $E_B \approx 120\,\mathrm{nK} = 2.5\,\mathrm{kHz}$
- Temperature $T \approx 60\,\mathrm{nK} = 1.3\,\mathrm{kHz}$

Therefore, the phase plate was ordered to have a trapping frequency of at least $\omega_z/2\pi = 30\,\mathrm{kHz}$, much larger that all the other energy scales.

Chapter 3

Characterization of the phase plate

The final goal of this project was to have a complete characterization of the phase plate that we received from the company. We knew its expected behaviour, namely the creation of a top hat potential with the characteristics described in Section 2.2.2. However, it is important to test any new components, to see how they behave in reality.

3.1 Building the experimental setup

3.1.1 Imaging system

In order to characterize the phase plate, the first step was to set up an imaging system. This was necessary to acquire images of the intensity distribution generated by our spatial light modulating system. Since the expected dimensions of the intensity distribution were of the order of 10 µm, a magnification system was set up. The magnification system is composed by a microscope objective, which magnifies the beam, and by a CCD camera. The distance between the two is kept constant by fixing everything in a cage. The objective can be aligned to the beam moving it in the horizontal (y) and vertical (z) direction by turning two micrometers. A sketch of the setup is shown in Fig. 3.1. The whole system (objective+camera) was mounted on a linear translation stage, with which it could be moved along the x direction to find the focus.

In order to use the imaging system to take measurements, it had to be calibrated. For the calibration, a laser beam was sent to a target like the one shown in Fig. 3.2a and imaged. From the image shown in Fig. 3.2b, it was possible to calculate the magnifying power of the imaging system. The lines were measured to be separated by 413(2) µm. Knowing that on the target the separation was 1/55 mm, we find a magnifying power of 22.7(1).

3.1.2 Test with the $0 - \pi$ phase plate

Before testing the top hat phase plate, the setup was tried with the $0-\pi$ phase plate currently used. In this previous setup, the laser beam coming from a fiber is collimated with a single lens. The beam is then magnified in the z direction by a telescope made of two cylindrical lenses

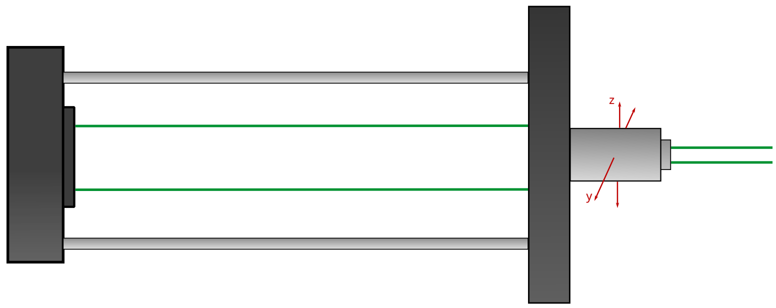

Figure 3.1: *Imaging system. A microscope objective magnifies the image and a CCD camera acquires it. The objective can be moved in the y and z direction with two micrometers.*

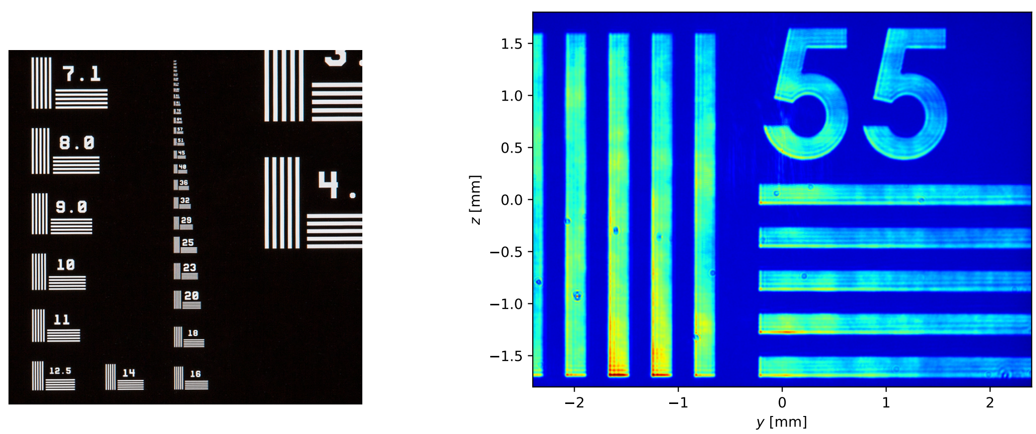

(a) *Target* **(b)** *Magnified image*

Figure 3.2: *Calibration of the imaging system. On the left, an example of a target similar to the one used in the experiment. On the right, the magnified image of a portion of the target. The number 55 means that the target has 55 lines / mm.*

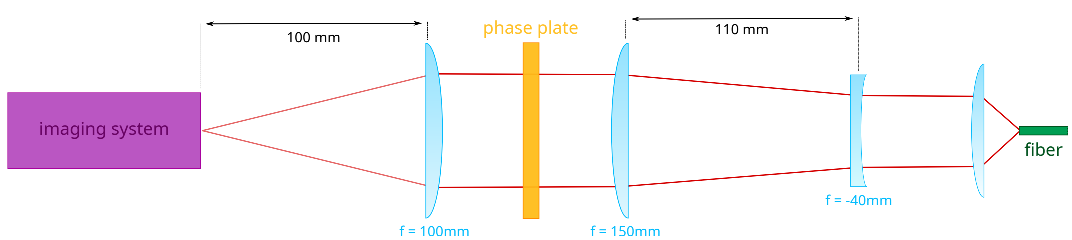

Figure 3.3: *Setup for the test of the $0-\pi$ phase plate. The beam coming from the fiber is collimated by a single lens, then expanded by two cylindrical lenses and sent to the phase plate. After the phase plate, an $f = 100\,\mathrm{mm}$ lens is placed and the result is imagined at the focal plane of the last lens. The two cylindrical lenses and the phase plate are mounted on a rotation mount.*

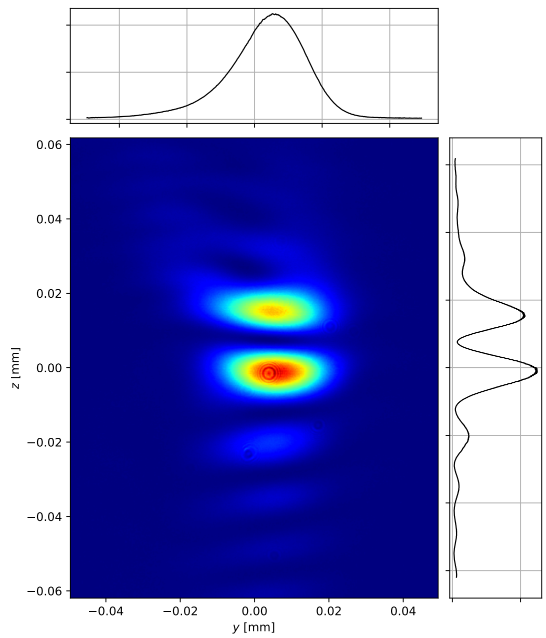

Figure 3.4: *Intensity distribution after the $0-\pi$ phase plate. The size shown on the axis is the real size of the beam. The plots on the right and on top of the image show the integrated sum of the intensity along the respective axes.*

($f = -40/150$ mm) placed 110 mm apart. The magnification of the beam helps to achieve higher trapping frequencies. The beam is then sent to the phase plate and an $f = 100$ mm lens. The two cylindrical lenses and the phase plate are mounted on a rotation mount, to allow the alignment of their axis. The result is imaged by the imaging system at the focal plane of the last lens. The focus is adjusted by moving the imaging system along the x direction with a micrometer. A sketch of this setup is shown in Fig. 3.3.

In order to get a good result, it is important that the two cylindrical lenses and the phase plate axes are aligned. To align it, the beam was observed at short and long distances. Acting on the first lens, the beam was rotated in a way such that its axis was aligned vertically. The same alignment was then performed acting on the second cylindrical lens and looking at the beam in the far field. The procedure was repeated, "walking" the beam, until the two lenses were aligned. The collimation of the beam was ensured by using a shear plate. Finally, the phase plate was aligned rotating its axis in such a way that it was parallel to the beam axis and moving it up or down such that the intensity of the two peaks was the same.

The final result is shown in Fig. 3.4. The result resembles the expected TEM_{01} mode shown in Fig. 2.2b, but it is clear that it could be optimized and made more symmetric. In particular, the alignment of the whole setup could have been improved. However, since the characterization of the $0-\pi$ phase plate was not the goal of the project, the setup was not optimized. Nonethss, this test was useful to gain familiarity on how to work with phase plates, before studying the one we were interested in.

3.1.3 Shaping the input beam

It had already been reported in Schmidt's work that the most crucial parameter to make the phase plate work is the beam diameter [14]. The phase plate was ordered for a diameter of 6 mm, so this is the first thing we tried to achieve.

Single collimating lens + x2 telescope

Initially we tried to collimate the beam coming from the fiber with a single lens with a focal length chosen to produce a 3 mm beam. Using a $\times 2$ telescope, composed of a $f = 50$ mm and a $f = 100$ mm achromatic lenses placed 150 mm apart, we expected a final beam with a diameter of 6 mm. We first tried to collimate the beam with 15.3 mm C260-TME-A lens (Fig. 3.5a), but the beam was smaller than 3 mm. Then we tried two 18.4 mm lens (Figs. 3.5b and 3.5c). The diameter of the former (C280-TMD-A) was too small (≈ 3 mm), and produced a beam with many aberrations; the latter, with a larger diameter, seemed to solve the problem. The beam was then magnified by the telescope, resulting in the picture shown in Fig. 3.5d.

Given the bad result, we decided to try with a different configuration.

Schäfter-Kirchhoff collimator + $\times 3$ telescope

The second configuration we tried we collimated the beam with a Schäfter-Kirchhoff collimator (60FC-4-M12-10, $f = 12$ mm). The collimator was expected to produce a beam with a diameter of ≈ 2 mm, which therefore required a $\times 3$ telescope. The telescope was assembled using a -50 mm lens and a 150 mm lens. Both lenses were achromatic lenses, to reduce aberrations. The use of a concave and a convex lens, beside reducing aberrations, allowed also to keep the setup more compact. The beams before and after the telescope are shown in Figs. 3.6a and 3.6b.

In Fig. 3.6c it is also shown the profile of the beam after being shaped by the phase plate in combination with a 100 mm lens. It is clear that, despite the general features of the top hat distribution being present, the intensity distribution is very different from the expected one. In particular the top and bottom light sheets seem to be curved around the centre.

Single collimating lens

To improve the previous result, we tried to reduce the aberrations using a single achromatic lens to collimate the beam directly to the desired size. In particular, we tried two different lenses: TRH254-040-A-ML ($f = 40$ mm) and MG 01LAO785 ($f = 37.5$ mm). The results are shown in Fig. 3.7. Also in this configuration, the beam differs a lot from a clean Gaussian beam.

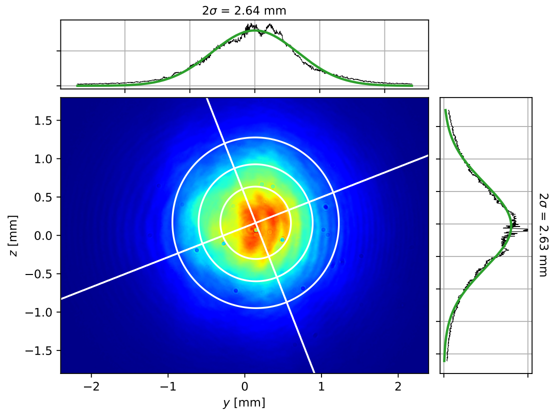

(a) $f = 15.3\,\mathrm{mm}$

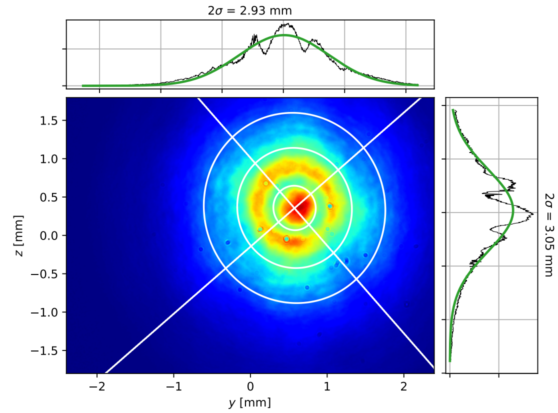

(b) $f = 18.4\,\mathrm{mm}$, *small diameter*

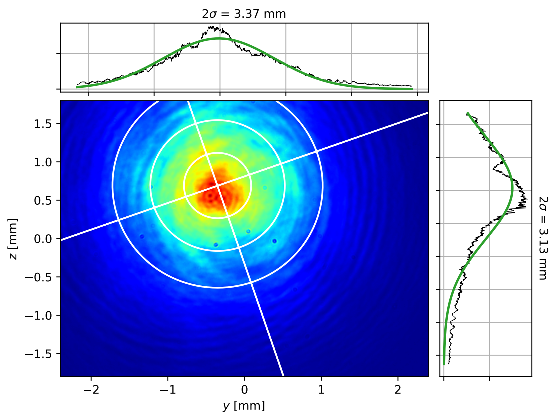

(c) $f = 18.4\,\mathrm{mm}$, *large diameter*

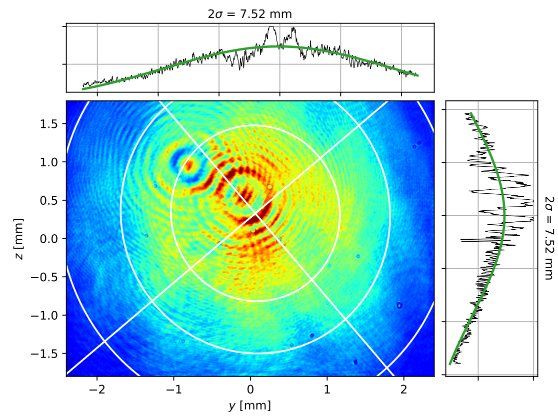

(d) $f = 18.4\,\mathrm{mm}$, *x2 telescope*

Figure 3.5: *Beam collimation with a single lens. The focal length of each lens is indicated below the respective figure. In figure (b) and (c) the lenses have the same focal length but different diameter. In figure (d) the beam is magnified with a* $\times 2$ *telescope.*

Schäfter-Kirchhoff collimator

Since we were not able to achieve good results only with the optics we had in the lab, we decided to order a collimator with the desired features. In particular, we ordered a Schäfter-Kirchhoff 60FC-L-4-M35-26 collimator, specifically designed to collimate large beams. In Fig. 3.8 we show the beam and the result after it being shaped by the phase plate together with a 100 mm lens. Surprisingly, the result is even worse than the previous ones. Placing the phase plate in the far field with respect to the collimator, the result does not change appreciably. Even trying to reduce the aberrations by adding a 1:1 telescope with a pinhole in between, the result remained the same.

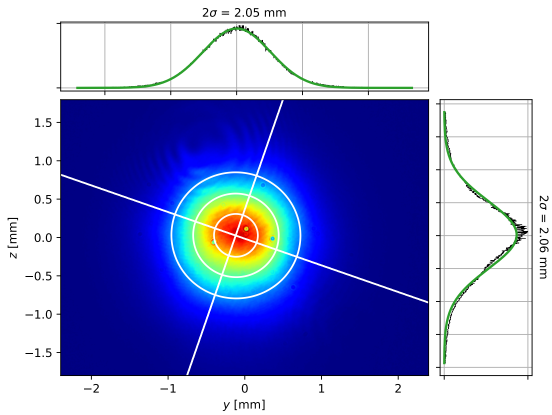

(a) $f = 12\,\mathrm{mm}$

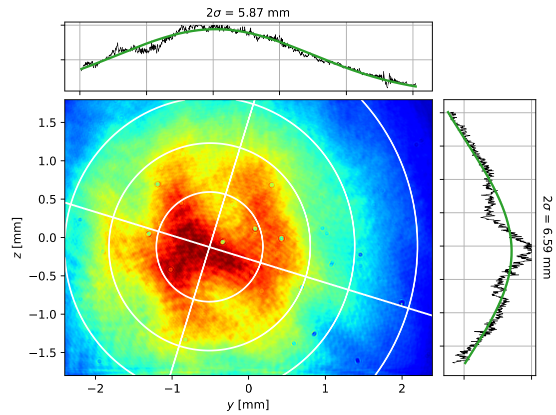

(b) $f = 12\,\mathrm{mm}$, $\times 3$ *telescope*

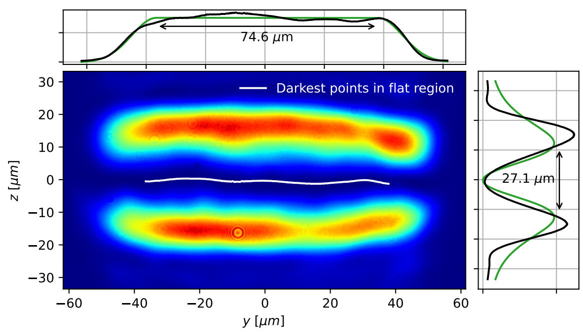

(c) *Top hat distribution*

Figure 3.6: *Beam collimation with a* 12 mm *Schäfter-Kirchhoff collimator, magnified with a* $\times 3$ *telescope ((a) and (b)). The meaning of the fits in (c) are explained Section 3.2.1.*

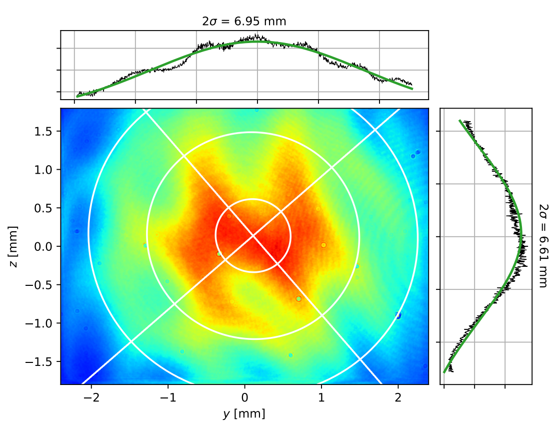

(a) $f = 40\,\mathrm{mm}$

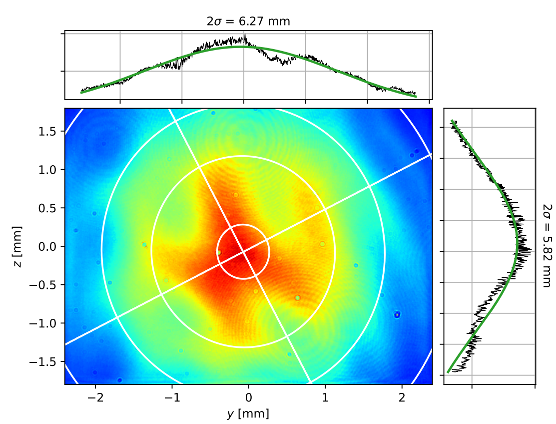

(b) $f = 37.5\,\mathrm{mm}$

Figure 3.7: *Beam collimation with a single lens.*

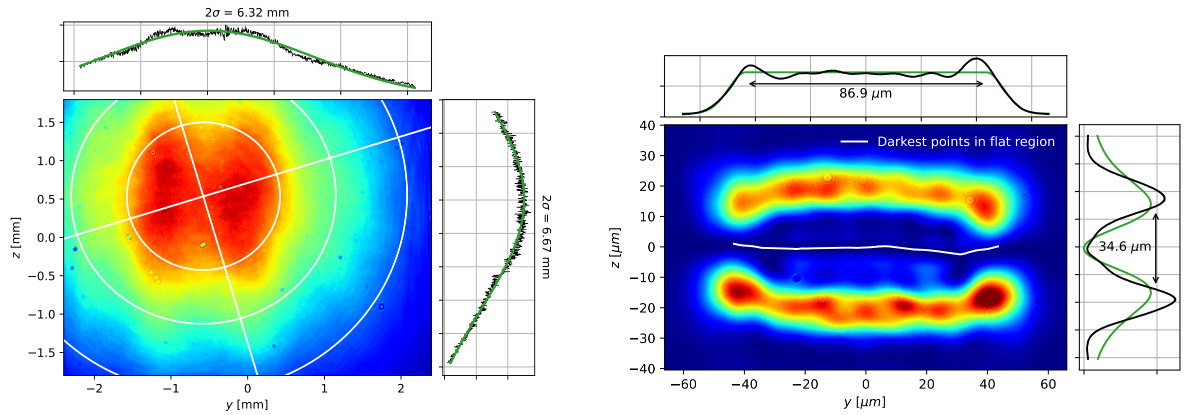

(a) *Beam* **(b)** *Top hat*

Figure 3.8: *Beam collimation with a Schäfter-Kirchhoff* 35 mm *collimator. The first image shows the beam after the collimator. The second image shows the top hat distribution generated by the phase plate together with a* 100 mm *lens. The meaning of the fits in (b) are explained Section 3.2.1.*

Schäfter-Kirchhoff collimator + ×3 telescope with varying size

Since even in the (theoretically) best configuration, i.e. using a collimator designed to produce a beam of the desired size, the result was far from optimal, we thought that the problem may have been in the beam size itself. Therefore, we decided to investigate the influence of the beam diameter on the result more systematically. To do so, we went back to the configuration with the chäfter-Kirchhoff 12 mm collimator with the ×3 telescope, with which we had obtained the best result so far.

To vary the size of beam, instead of using the collimator in its usual way, we manually adjusted it to produce a non-collimated beam. Moving the second lens of the telescope back and forth, it was then possible to re-collimate the beam. In this way, we could vary the size of the beam keeping it collimated at the phase plate position.

The results, for three different sizes of the beam, are collected in Fig. 3.9. From the figures, it is clear that the dimension of the beam has a big influence on the result. Even changes of fractions of a millimetre produce great differences in the final result. In particular, it is interesting to observe that for large beams we recognize the behaviour observed in all the previous configurations, i.e. a curvature of the two peaks around the centre. On the other hand, small beams produce an uneven intensity distribution along the y axis, with peaks at the border of the flat region. A good compromise seems to be found for a beam of ≈ 5 mm. This explains the bad results obtained before, since we were using much larger beams, even if the size was similar to the specifications given by the manufacturing company.

Having found a good beam size which we could aim for, we decided to build a telescope that would give us approximately the desired size, and use it to fully characterize the phase plate.

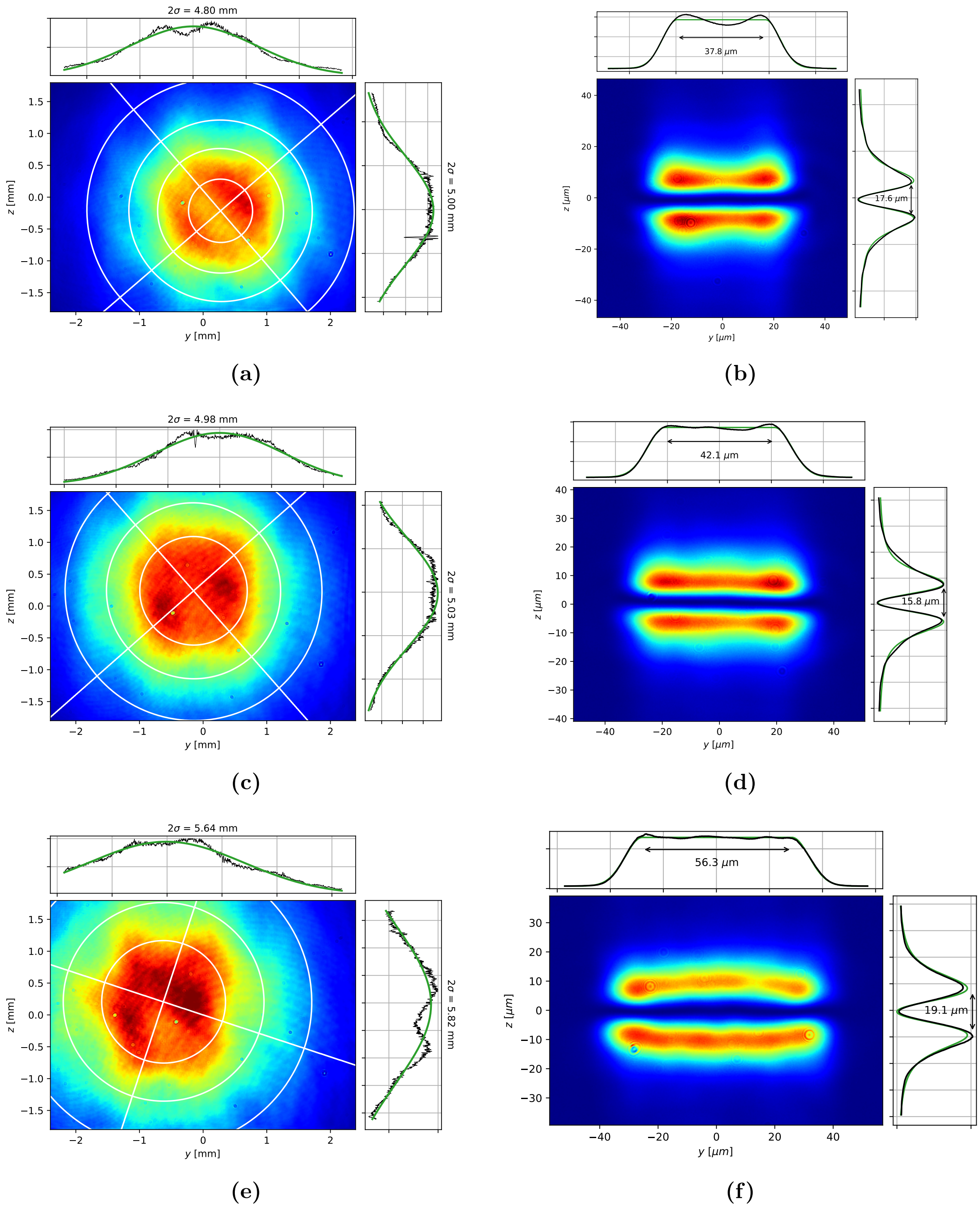

Figure 3.9: *Beam and top hat distribution for different beam sizes. Every row shows a beam on the left and its respective top hat distribution on the right. The results were obtained with the 12 mm collimator and together with the ×3 telescope. The meaning of the fits on the top hat images are explained Section 3.2.1.*

3.2 Characterization

For the characterization of the phase plate we decided to keep using the Schäfter-Kirchhoff 12 mm collimator, but instead of magnifying the beam with a $\times 3$ telescope, we used a $\times 2.5$ telescope. With this setup, we expected a beam with a diameter of ≈ 5 mm, size for which we had previously found the best results. The telescope was built with a -50 mm and a 120 mm achromatic lenses.

3.2.1 Methods

For a complete characterization of the phase plate, it was necessary to analyse its behaviour for different beam sizes and different distances from the focus. It is important to look at the light sheet at different distances from the focus because, despite the focal point being in principle well-defined, it is non-trivial to find it. Moreover, it may happen that for our goals a non-perfectly focused beam is better than a focused one.

Intensity normalization

For every combination of beam size and distance from the focus, two pictures were taken: a normal (non-satuaretd) picture and a saturated picture. The non-satuaretd picture gives us information on the intensity distribution for the whole light sheet. The saturated picture allows us to increase the dynamic range in the dark region at the centre, allowing more precise measurements. An example of a saturated picture can be found in Fig. 3.10a. To saturate the picture we increased the exposure time. Taking note of both the exposure time of the saturated picture and of the non-satuaretd one, it was possible to "normalize" the saturated picture as

$$I_{\mathrm{s}}^{\mathrm{norm}} = \frac{\tau_{\mathrm{ns}}}{\tau_{\mathrm{s}}} I_{\mathrm{s}} \tag{3.1}$$

where $\tau_{\mathrm{ns/s}}$ are respectively the exposure time of the non-saturated and saturated pictures, I_{s} the intensity measured by the camera for the saturated picture and $I_{\mathrm{s}}^{\mathrm{norm}}$ the normalized intensity.

For both pictures, the absolute intensity I_{abs} was found scaling the intensity measured by the camera I_{rel} (already normalized for the saturated image) with a factor given by the power of the laser P divided by the total power measured by the camera

$$I_{\mathrm{abs}}(y, z) = P \frac{I_{\mathrm{rel}}(y, z)}{\int \mathrm{d}y' \mathrm{d}z' I_{\mathrm{rel}}(y', z')} \tag{3.2}$$

For all the following calculations, we assumed to have a laser with a power of 1 W.

Global behaviour

The expected intensity distribution generated by the phase plate $I(y, z) = I_{\mathrm{th}}(y) I_{0\pi}(z)$ is given by a top hat distribution $I_{\mathrm{th}}(y)$ in the y direction and by a $0 - \pi$ distribution $I_{0\pi}(z)$in the z direction. The top hat distribution is given by

$$I_{\text{th}}(y) = \begin{cases} \exp\left[-\left(\frac{|y|-w_F}{w_R}\right)^2\right] & |y| > w_F \\ 1 & |y| \leq w_F \end{cases} \tag{3.3}$$

where we have defined $2w_F$ as the length of the flat region and w_R the length of the ramp-up. The $o - \pi$ distribution is given by

$$I_{0\pi}(z) = \text{erfi}\left[\frac{z}{w_e}\right]^2 \exp\left[-2\left(\frac{z}{w_e}\right)^2\right] \tag{3.4}$$

where $\text{erfi}(z) = -i\,\text{erf}(iz)$ is the imaginary error function and w_e an appropriate length scale. It is possible to notice that the erfi distribution has two peaks distanced by $2w$.

Since the two variable (y, z) of the intensity distribution $I(y, z)$ are theoretically independent, we can gain some first information looking at the integrated sum of the intensity along the two axis

$$I_z(y) = \int \mathrm{d}z' I(y, z') \tag{3.5}$$

$$I_y(z) = \int \mathrm{d}y' I(y', z) \tag{3.6}$$

fitting the respective distributions $I_{\text{th}}(y)$ and $I_{0\pi}(z)$. This is what was done, for example, in Fig. 3.9d, where we found a flat region length $2w_F$ of 42.1 µm and an erfi distribution with the two peaks distanced by $2w_e = 19.1$ µm.

The integrated intensity $I_z(y)$ can also be used to calculate a first quantity useful to quantify the "flatness" of the top hat, the so-called peak-to-peak (P2P). The P2P is simply defined as the minimum intensity in the flat region divided by the maximum

$$\text{P2P} = \min_y(I_z(y))/\max_y(I_z(y)) \qquad |y| < w_F \tag{3.7}$$

The closer the P2P is to one, the flatter the top hat distribution is.

Local behaviour

Even if the previous analysis give us a good understanding of the global characteristic of the intensity distribution, it fails to be precise about the exact behaviour at the point we are mostly interested in: the central region. Since the atoms will be trapped in this region, ideally in a 2D space, they will only feel the local potential near $z = 0$. It is therefore important to characterize this region with more precision.

We have already mentioned in Section 2.2.3 that two important quantities for the characterization of the phase plate are the darkness D, defined in Eq. (2.17), and the trapping frequency ω_z, defined in Eq. (2.18). If these two quantities are evaluated for every y, their mean and their variation will give us information on the darkness of the region, on the strength of the trapping potential and on the uniformity of the intensity.

To compute these quantities, using the saturated picture, we fit a parabola for every y. We can then use the quadratic coefficient to compute the trapping frequency and the height of the vertex to compute the darkness. An example is shown in Fig. 3.10.

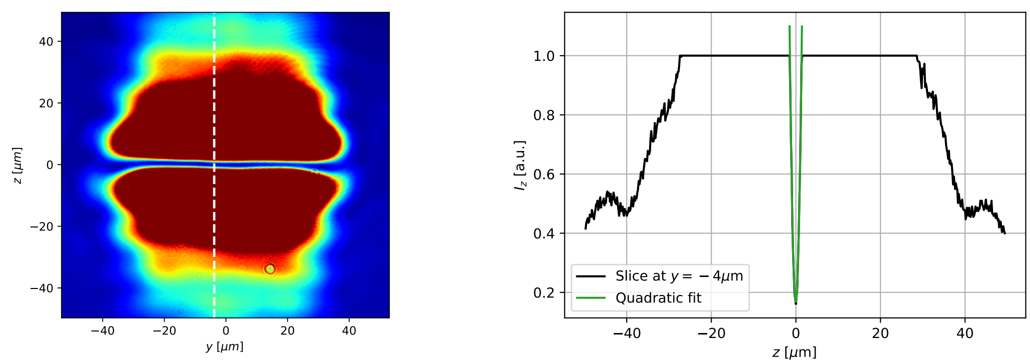

(a) *Saturated image* **(b)** *Quadratic fit*

Figure 3.10: *Example of the quadratic fit of a slice of a saturated image. The slice is taken at* $y = -4\,\mu\mathrm{m}$.

Acknowledgements

Bibliography

[1] Immanuel Bloch, Jean Dalibard, and Sylvain Nascimbène. "Quantum Simulations with Ultracold Quantum Gases". In: *Nature Physics* 8.4 (4 Apr. 2012), pp. 267–276. ISSN: 1745-2481. DOI: 10.1038/nphys2259 (cit. on p. 1).

[2] Richard P. Feynman. "Simulating Physics with Computers". In: *International Journal of Theoretical Physics* 21.6 (June 1, 1982), pp. 467–488. ISSN: 1572-9575. DOI: 10.1007/BF02650179 (cit. on p. 1).

[3] Alexandre Blais et al. "Circuit Quantum Electrodynamics". In: *Reviews of Modern Physics* 93.2 (May 19, 2021), p. 025005. ISSN: 0034-6861, 1539-0756. DOI: 10.1103/RevModPhys.93.025005 (cit. on p. 1).

[4] Xiaoling Wu et al. "A Concise Review of Rydberg Atom Based Quantum Computation and Quantum Simulation*". In: *Chinese Physics B* 30.2 (Feb. 2021), p. 020305. ISSN: 1674-1056. DOI: 10.1088/1674-1056/abd76f (cit. on p. 1).

[5] Colin D. Bruzewicz et al. "Trapped-Ion Quantum Computing: Progress and Challenges". In: *Applied Physics Reviews* 6.2 (May 29, 2019), p. 021314. ISSN: 1931-9401. DOI: 10.1063/1.5088164 (cit. on p. 1).

[6] Immanuel Bloch, Jean Dalibard, and Wilhelm Zwerger. "Many-Body Physics with Ultracold Gases". In: *Reviews of Modern Physics* 80.3 (July 18, 2008), pp. 885–964. ISSN: 0034-6861, 1539-0756. DOI: 10.1103/RevModPhys.80.885 (cit. on p. 2).

[7] Felix Bloch. "Über die Quantenmechanik der Elektronen in Kristallgittern". In: *Zeitschrift für Physik* 52.7 (July 1, 1929), pp. 555–600. ISSN: 0044-3328. DOI: 10.1007/BF01339455 (cit. on p. 2).

[8] Maxime Ben Dahan et al. "Bloch Oscillations of Atoms in an Optical Potential". In: *PHYSICAL REVIEW LETTERS* 76.24 (1996) (cit. on p. 2).

[9] J. Feldmann et al. "Optical Investigation of Bloch Oscillations in a Semiconductor Superlattice". In: *Physical Review B* 46.11 (Sept. 15, 1992), pp. 7252–7255. DOI: 10.1103/PhysRevB.46.7252 (cit. on p. 2).

[10] Markus Greiner, Olaf Mandel, and Tilman Esslinger. "Quantum Phase Transition from a Super¯uid to a Mott Insulator in a Gas of Ultracold Atoms". In: 415 (2002) (cit. on p. 2).

[11] Renate Landig et al. "Quantum Phases from Competing Short- and Long-Range Interactions in an Optical Lattice". In: *Nature* 532.7600 (7600 Apr. 2016), pp. 476–479. ISSN: 1476-4687. DOI: `10.1038/nature17409` (cit. on p. 2).

[12] Sebastian Krinner et al. "Observation of Quantized Conductance in Neutral Matter". In: *Nature* 517.7532 (7532 Jan. 2015), pp. 64–67. ISSN: 1476-4687. DOI: `10.1038/nature14049` (cit. on p. 2).

[13] Sebastian J. Krinner. "Quantum Transport of Ultracold Atoms". Doctoral Thesis. ETH Zurich, 2015. DOI: `10.3929/ethz-a-010556528` (cit. on pp. 2, 3, 9).

[14] Moritz Fontboté Schmidt. "Towards a Uniform Two-Dimensional Channel for Transport Experiments with Ultracold Gases". ETH Zürich, Feb. 17, 2021 (cit. on pp. 3, 6, 8, 15).

[15] Bahaa E. A. Saleh and Malvin Carl Teich. "Fourier Optics". In: *Fundamentals of Photonics*. John Wiley & Sons, Ltd, 1991, pp. 108–156. ISBN: 978-0-471-21374-1. DOI: `10.1002/0471213748.ch4` (cit. on p. 6).

[16] Ruth Heine. "Digital In-Line x-Ray Holographic Microscopy with Synchrotron Radiation". In: (Jan. 2008) (cit. on p. 7).